

Global instability of compressor rotating stall onset

Shenren Xu ^{*1}, Chen He^{†2}, Dakun Sun^{‡2}, Sebastian Timme^{§3}, and Dingxi Wang^{¶1}

¹*Northwestern Polytechnical University, Taicang 215400, P.R. China*

²*Beihang University, Beijing 100191, P.R. China*

³*University of Liverpool, Liverpool xxx, United Kingdom*

Rotating stall taking place at the low-mass-flow side of the compressor map directly determines the compressor's working range

Linear global stability analysis is an effective approach to predict the exact condition at which flow goes unstable. Compared to the time-domain simulation approach, ??? method can equivalently predict the destabilization condition, but at a much lower cost, since unsteady simulations are no longer required. In this work, a Newton–Krylov nonlinear flow solver is used to first solve for the steady state flow solution and then eigenanalysis is performed by applying the implicit-restart Arnoldi method to the exact Jacobian matrix. By tracking a subset of the eigenspectrum that is close to the imaginary axis, the least stable eigenmodes can be found. By perturbing the bifurcation parameter, e.g., the Reynolds number, the Hopf bifurcation point can be identified. This method is applied to find the critical Reynolds number for a laminar flow around a circular cylinder above which laminar vortex shedding appears. Time-accurate unsteady simulation confirms the correctness of the critical eigenvalue and eigenvector found. It is also applied to a quasi-3D compressor rotor annular cascade case, for which eigenanalysis is performed and flow physics is analyzed based on the unstable modes identified. Interesting correlation between the rotating perturbation pattern and cell rotating speed is found, which resembles what is observed in experiments. This work is a first step towards the study of rotating flow instabilities in turbomachines, such as rotating stall and rotating instability, and the preliminary results proved promising for future application to three-dimensional practical problems.

Nomenclature

c_v, c_p = specific heat

e = internal energy

^{*} Associate Professor, Yangtze River Delta Research Institute

[†] Ph.D. Candidate, School of Energy and Power Engineering; hechen@buaa.edu.cn

[‡] Associate Professor, School of Energy and Power Engineering; sundk@buaa.edu.cn

[§] Senior Lecturer, School of Engineering; sebastian.timme@liverpool.ac.uk

[¶] Professor, School of Power and Engery; dingxi_wang@nwpu.edu.cn

E = total energy

$\partial\Omega_r$ = boundary of Ω_r

NASA R67 eigenanalysis to-do list

- 1) survey stations 1-2 performance data
- 2) ND=0 eigenvalues for 18kpa through 23kpa
- 3) single passage URANS for unstable case
- 4) other ND eigenvalues (phase shift bc)
- 5) full annulus URANS for unstable case

I. Introduction

II. Numerical approach

The flow is computed using the NutsCFD solver, whose accuracy has been validated intensively for axial and centrifugal compressors [1]. The RANS equations are discretized using the finite volume method on arbitrary unstructured meshes. The inviscid flux is calculated with Roe's flux difference splitting scheme and the viscous flux is calculated using central scheme. Second-order accurate spatial discretisation is achieved via linear reconstruction of the primitive variable from the mesh node to the flux face center and the gradient of flow variables are obtained using the Green-Gauss approach. Simulation of the unsteady flow for a rotating geometry is converted to the computation of a steady flow by re-formulating the governing equations in a reference frame coindending with the rotating geometry. In order to obtain a steady flow as the base-flow for linearizing the perturbed flow about and performing eigenvalue analysis, at physically unstable states, a globalized Newton–Krylov approach is used to integrate the unsteady RANS equations in time. This is one of the key technical enablers for performing global instability analysis for compressors beyond stall.

The nonlinear flow solver used in this work is NutsCFD, an unstructured-mesh finite-volume RANS solver capable of dealing with rotating frame reference and periodic boundary conditions. The solver features the use of the Newton–Krylov algorithm, which significantly enhances the efficiency and robsutness when computing turbomachinery flows at off-design conditions. Details of the solver can be found in and a brief description of the solution algorithm is provided in this section.

A. Governing equations

The integral form of the governing equations in a relative frame of reference with a constant angular velocity of ω is

$$\frac{d}{dt} \int_{\Omega_r} \mathbf{W} dV + \oint_{\partial\Omega_r} (\mathbf{F}_c^r - \mathbf{F}_v) dS + \int_{\Omega_r} \mathbf{F}_\omega dV = 0,$$

where \mathbf{W} are the conservative variables $[\rho, \rho\mathbf{u}, \rho E]^T$. The absolute and relative convective fluxes, \mathbf{F}_c and \mathbf{F}_c^r , the viscous flux \mathbf{F}_v , and the additional source term due to rotation, \mathbf{F}_ω , are defined as

$$\mathbf{F}_c = \begin{bmatrix} \rho\mathbf{u} \cdot \mathbf{n} \\ \rho\mathbf{u}\mathbf{u} \cdot \mathbf{n} + p\mathbf{n} \\ \rho H\mathbf{u} \cdot \mathbf{n} \end{bmatrix}, \quad \mathbf{F}_c^r = \mathbf{F}_c - (\mathbf{u}_{rot} \cdot \mathbf{n}) \begin{bmatrix} \rho \\ \rho\mathbf{u} \\ \rho E \end{bmatrix}, \quad \mathbf{F}_v = \begin{bmatrix} 0 \\ \boldsymbol{\tau} \cdot \mathbf{n} \\ \mathbf{u} \cdot \boldsymbol{\tau} \cdot \mathbf{n} + \kappa \mathbf{n} \cdot \nabla T \end{bmatrix}, \quad \mathbf{F}_\omega = \begin{bmatrix} 0 \\ \rho\boldsymbol{\omega} \times \mathbf{u} \\ 0 \end{bmatrix},$$

with $\mathbf{u}_{rot} = \boldsymbol{\omega} \times \mathbf{x}$. When $\boldsymbol{\omega}$ is zero, a solver applicable to non-rotating reference frame is recovered.

Flow is assumed to be fully turbulent and turbulence is modeled using the negative Spalart–Allmaras (SA-neg) model [2]. Compared to the original SA model [3], this avoids the clipping of the turbulent variable to a non-negative value which potentially prevents the full convergence of the nonlinear solver. The turbulence equation is discretized using the first-order accurate upwind scheme [4].

B. Spatial discretization

The governing equations are discretized using the method of lines and thus the spatial and temporal discretizations can be treated separately. The governing equations for the steady-state solution \mathbf{W} is

$$\mathbf{R}(\mathbf{W}) = \mathbf{0}, \quad (1)$$

where \mathbf{R} is the sum of fluxes and source terms associated with each control volume. Suppose control volume i has N flux faces with area S_{ik} for $k = 1, 2, \dots, N$. R_i then is

$$R_i(\mathbf{W}) = \sum_{k=1}^N (\mathbf{F}_c^r - \mathbf{F}_v) S_{ik} + \mathbf{F}_\omega V_i,$$

where V_i denotes the volume. The computation of the convective flux \mathbf{F}_c^r is based on a modification of the Roe flux scheme to account for the relative reference frame that is rotating with a constant angular velocity; while the viscous flux \mathbf{F}_v is the same as in the stationary reference frame.

C. Temporal discretization for steady solver

The Newton method solves the steady-state nonlinear equation (1) iteratively as

$$\mathbf{W}^{n+1} = \mathbf{W}^n + \beta \Delta \mathbf{W}$$

until convergence is reached, i.e., $\|\mathbf{R}(\mathbf{W})\| = 0$, where $\Delta\mathbf{W}$ is the solution to the linear system of equations

$$\frac{\partial \mathbf{R}}{\partial \mathbf{W}} \Delta \mathbf{W} = -\mathbf{R}(\mathbf{W}^n),$$

while β is an under-relaxation factor obtained using a line search.

Once the spatial discretization, $\mathbf{R}(\mathbf{W}^n)$, is established, there are three main steps to complete a Newton update step, namely, (i) forming the Jacobian matrix, (ii) solving the large sparse linear system of equations, and (iii) finding a step size β and update the nonlinear flow solution. To form the Jacobian matrix, automatic differentiatino tool Tapenade [5] is used, together with graph coloring tool Colpack [6]. By executing the foward-differentiated residual subroutine for a subsets of nodes with the same color, the Jacobian matrix is calculated. The resulting large sparse linear system of equations is solved using GMRES right-preconditioned by the incomplete LU factorization with zero fill-in.

D. Temporal discretization for unsteady solver

III. Global linear stability analysis via eigenmode decomposition

A. Global linear stability analysis

B. Numerical implementation of eigenanalysis

In theory, performing the global linear stability analysis as described above is a standard procedure involving three steps: (i) find an equilibrium point \mathbf{u}_0 ; (ii) linearize the nonlinear residual and form the Jacobian matrix A , and (iii) perform eigenanalysis and find Λ and V . Step (i) is simply running the steady state flow solver until a steady state solution is found. Step (ii) is a by-product of the nonlinear flow calculation using the NK method, i.e., store away the Jacobian matrix at the final Newton step. Step (iii) is a bit more involved for high dimensional problems.

For eigenmode computations, the implicitly restarted Arnoldi method proposed by Sorensen [7] and implemented in the ARPACK library [8], is used in combination with the NutsCFD solver. Shift-and-invert spectral transformation is applied to converge to wanted parts of the eigenspectrum, and critical is therefore the robust solution of many linear systems of equations. Key to efficiently solving the arising large sparse linear system of equations is the deflated Krylov subspace solver GCRO-DR [9]. Compared with the more commonly used GMRES solver [10], GCRO-DR is both more CPU time and memory efficient, especially as the system matrix condition worsens, as demonstrated in [11, 12].

IV. Results

A. Laminar flow vortex shedding

Steady, unsteady and eigenvalue analysis is performed for two-dimensional laminar flows around a circular cylinder with Reynolds number between 30 and 100. The computational domain is a $200m \times 200m$ square with a circular

cylinder of diameter $D = 2m$ centered at the origin. The computational domain is meshed with quadrilateral elements, with 51,480 grid points in total. Far-field boundary condition with total pressure $101325Pa$, total temperature $288K$ and a Mach number of 0.1 is applied at the left far-field boundary. Symmetric plane boundary condition is applied at the bottom and top boundaries. A constant back pressure of $101325Pa$ is applied at the right boundary. No-slip viscous wall boundary condition is applied at the surface of the circular cylinder. The dynamic viscosity is varied between $\mu = 2.779$ and $\mu = 0.8337Pa \cdot s$ to obtain Reynolds number between 30 and 100.

Steady state flow solutions are obtained using fully implicit steady solver based on the globalized Newon-Krylov scheme with the initial Courant number set to 100, for Reynolds numbers of 30, 40, 45, 50, 60, 80, and 100. Steady state is found when the residual of the continuity equation is reduced by ten orders of magnitude. The convergence history of all the steady calculations are shown in Fig. 1. All solutions are found with 40 nonlinear iterations.

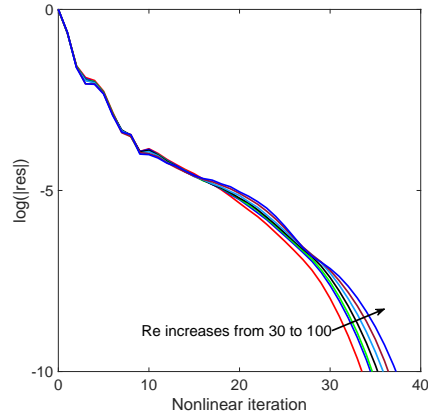


Fig. 1 Convergence history of steady flow calculations at different Reynolds numbers.

Eigenanalysis based on the implicitly restarted Arnoldi method is performed for the each steady flow solution. In particular, the ARPACK package is used with the shift-invert mode, which can efficiently calculate a small set of eigenvalues for large system matrices requiring minimal storage. In order to use the shift-invert mode, complex shift approximating the main frequency content of the physical problem is needed, to aim the search for eigenvalues. For this particular case,, thanks to the prior knowledge that the Strouhal number (St) is around 0.2, different imaginary shifts from $0i$ to $1i$ are applied to identify the relevant eigenvalues. The partial spectra are shown in Fig. 2. The abscissa is labelled "growth rate", which is the real part of the eigenvalue; while the ordinate is labelled "Strouhal number", which is converted from the imaginary part of the eigenvalue, which is also the angular frequency.

Due to the known symmetry of the spectra for real matrices, only the upper half of the spectra is computed and shown. It can be seen that when the parameter Re is varied from 30 to 100, most eigenvalues hardly move, except one that obviously breaks away from the bulk, and moves fast towards the positive half of the complex plane. This particular eigenvalue is marked and highlighted in the right half of Fig. 2 to illustrate its continuous tracing. When this eigenvalue

crosses the imaginary axis (the interpolated Re is approximately 48), the system becomes linearly unstable.

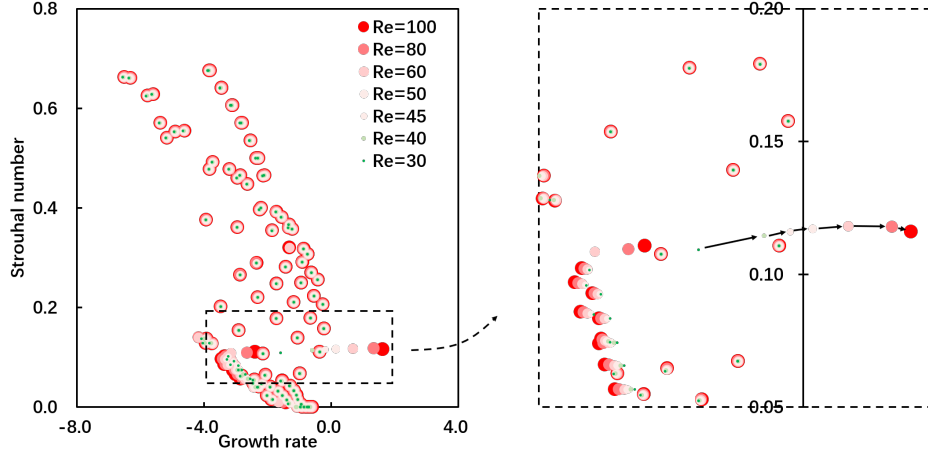


Fig. 2 123

Focusing on the single mode that destabilizes when Re increases, its dependence on the parameter Re is shown in Fig. 3, in terms of both the growth rate and the Strouhal number. The results are compared with other results from literature, which is also plotted in the figure. The critical Reynolds number for the bifurcation computed in our eigenvalue analysis is approximately $Re_{crit} = 48$ and the corresponding Strouhal number is $St_{crit} = 0.11673$, which is close to other independently obtained results. The eigenvalue analysis performed in [13] predicts a critical Reynolds number of $Re_{crit} = 47$ and a Strouhal number of $St_{crit} = 0.116$. The experimental results obtained in [14] is also plotted in Fig. 3, which although does not provides the exact critical value, does, however, seems to intercept our numerical results at a slightly lower Reynolds number of $Re_{crit} \approx 45$. The deviation of the Strouhal number predicted by the eigenvalue analysis from the experimental data as the Reynolds number grows beyond the critical value is not unexpected, as the eigenvalue analysis is linear while the periodic vortex shedding is nonlinear. Nevertheless, the eigenvalue analysis accurately predicts the onset of the unsteadiness, both the critical system parameter, i.e., the Reynolds number, and the angular frequency.

To verify the eigenvalue analysis results, time-accurate unsteady analysis is performed for flow at $Re = 100$. The unstable steady state for this Reynolds number has a conjugate pair of destabilizing eigenvalues $\lambda_{1,2} = 1.6245 \pm 12.39i$, corresponding to a growth rate of 1.6245 and an angular frequency of 12.39 rad/s or a Strouhal number of 0.116. This steady state solution is used to initialize the unsteady simulation. To obtain the unsteady flow, the Navier–Stokes equations are integrated in time using the second-order backward differentiation formula. The Newton–Krylov approach is used for the inner iteration, with the Jacobian and preconditioning matrices formed only once at the beginning of the entire unsteady calculation. A total of 50 subiterations are taken at each physical time step, ensuring machine error convergence throughout the entire unsteady run. The physical time step used is $\Delta T = 0.001$ second and the total duration of the simulation is 25 seconds. Time-step sensitivity study has been performed to ensure adequate temporal

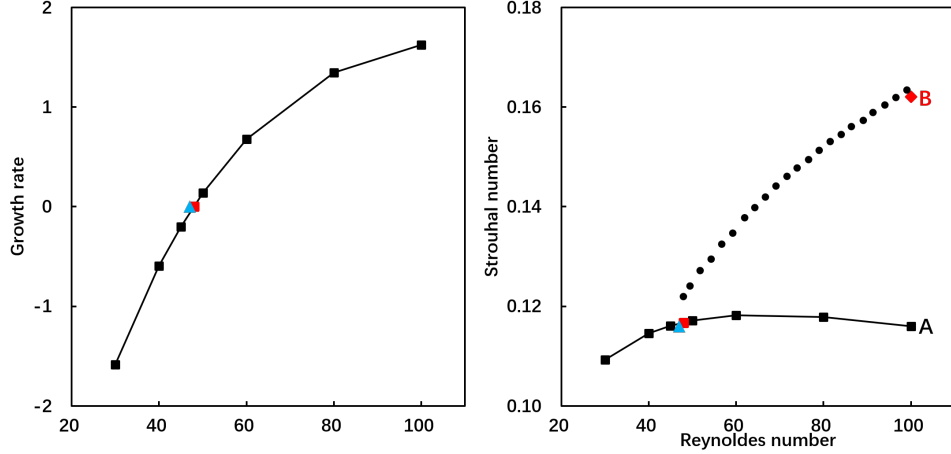


Fig. 3 The growth rate and strouhal number dependence on the Reynolds number. Black square: eigenvalue analysis results of this work; red square: critical condition from eigenvalue analysis results of this work; blue triangle: bifurcation point from the eigenvalue analysis in [13]; black circle: experimental data from [14].

precision is maintained. The flow for the unstable steady state (also the solution at $T = 0$ for the unsteady run) as well as the flow at the last time step of the unsteady run are shown in Fig. 4. The steady flow is reflection symmetric while the unsteady flow snapshot is non-symmetric and shows the vortex shedding.

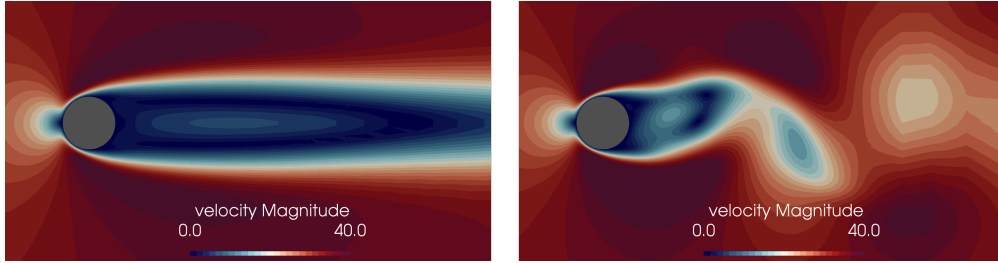


Fig. 4 Left: the velocity magnitude contour plot of the converged steady flow for $Re = 100$; right: the velocity magnitude contour plot of the unsteady flow snapshot at $T = 25sec$, exhibiting the vortex shedding. snapshot at the final step ($T = 25 sec$) of the unsteady run.

The lift coefficient during each physical time step is monitored and plotted for the duration of the unsteady simulation in Fig. 5. It can be seen that the lift coefficient, starting from essentially zero, exponentially grows for the first over 15 seconds before it levels out and reach a periodic solution with constant amplitude. The black solid curve in the left figure is with the form of $cl_{ROM} = c_0 e^{\lambda_1 t + i\phi} = c_0 e^{(1.6245 + 12.39i)t + i\phi}$ where c_0 and ϕ are the initial value and a phase shift that need to be determined via an optimization process that minimizes the error between the cl_{ROM} and the linear segment of the time-domain signal. To examine the frequency information of the time-domain signal, pseudo-angular frequency is obtained by taking the peak-to-peak interval of the cl signal is plotted again time in the right part of Fig. 5. Prior to $T = 18sec$, the angular frequency is $12.39rad/s$ and the Strouhal number is $St = 0.116$, corresponding to point A in Fig. 3. From $T = 18sec$ to $T = 20sec$, the angular frequency underwent a transient growth and in just around 10

periods, it increases to $\omega = 17.25 \text{ rad/s}$ ($St = 0.162$), corresponding to point B in Fig. 3. This frequency is very close to the experimental data and thus confirms that it is due to the non-linearity that the eigenvalue-based frequency diverges from the unsteady nonlinear flow. The frequency and growth rate of the unsteady flow in the linear perturbation regime, however, is accurately predicted by the eigenvalue analysis.

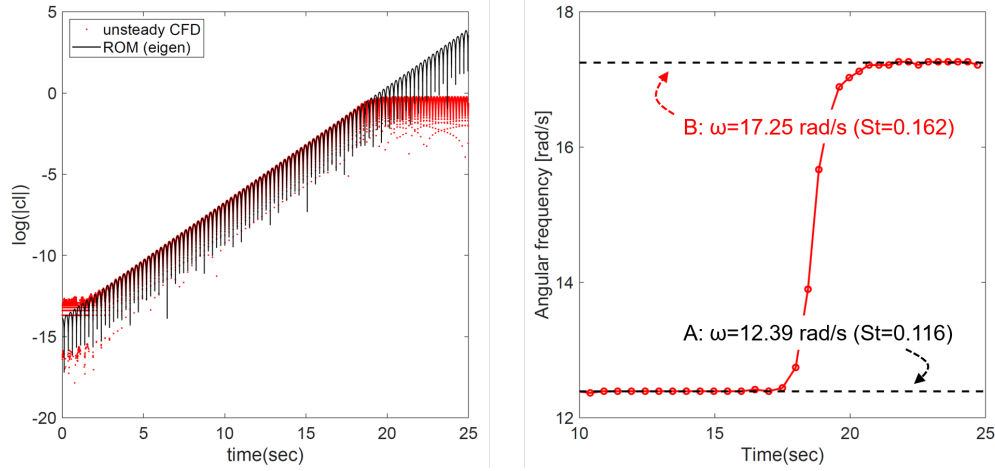


Fig. 5 Left: lift coefficient histogram for $Re = 100$ computed using unsteady solver from a converged unstable steady state, compared with the reduced-order-model (ROM) built using the unstable eigenmode; right: the pseudo angular frequency computed from the peak-to-peak interval of the time-domain lift coefficient signal.

This work received support by the National Natural Science Foundation of China (Grant No. 51790512).

References

- [1] Xu, S., Mohanamurthy, P., Wang, D., and Müller, J.-D., “Newton–Krylov Solver for Robust Turbomachinery Aerodynamic Analysis,” *AIAA Journal*, 2019, pp. 1–17.
- [2] Allmaras, S. R., and Johnson, F. T., “Modifications and clarifications for the implementation of the Spalart–Allmaras turbulence model,” *Seventh international conference on computational fluid dynamics (ICCFD7)*, 2012, pp. 1–11.
- [3] Spalart, P. R., and Allmaras, S. R., “A one equation turbulence model for aerodynamic flows,” *AIAA-CP 92-439*, 1992.
- [4] Langer, S., “Agglomeration multigrid methods with implicit Runge–Kutta smoothers applied to aerodynamic simulations on unstructured grids,” *Journal of Computational Physics*, Vol. 277, 2014, pp. 72–100.
- [5] Hascoët, L., and Pascual, V., “The Tapenade Automatic Differentiation tool: Principles, Model, and Specification,” *ACM Transactions On Mathematical Software*, Vol. 39, No. 3, 2013.
- [6] Gebremedhin, A. H., Nguyen, D., Patwary, M. M. A., and Pothen, A., “ColPack: Software for graph coloring and related problems in scientific computing,” *ACM Transactions on Mathematical Software (TOMS)*, Vol. 40, No. 1, 2013, p. 1.
- [7] Sorensen, D. C., “Implicit application of polynomial filters in a k-step Arnoldi method,” *SIAM journal on matrix analysis and applications*, Vol. 13, No. 1, 1992, pp. 357–385.

- [8] Lehoucq, R. B., Sorensen, D. C., and Yang, C., *ARPACK users' guide: solution of large-scale eigenvalue problems with implicitly restarted Arnoldi methods*, Vol. 6, SIAM, 1998.
- [9] Parks, M., de Sturler, E., Mackey, G., Johnson, D., and Maiti, S., "Recycling Krylov subspaces for sequences of linear systems," *SIAM Journal on Scientific Computing*, Vol. 28, No. 5, 2006, pp. 1651–1674.
- [10] Saad, Y., and Schultz, M., "GMRES: A generalized minimal residual algorithm for solving nonsymmetric linear systems," *SIAM Journal on scientific and statistical computing*, Vol. 7, No. 3, 1986, pp. 856–869.
- [11] Xu, S., Timme, S., and Badcock, K., "Enabling off-design linearised aerodynamics analysis using Krylov subspace recycling technique," *Computers & Fluids*, Vol. 140, 2016, pp. 385–396.
- [12] Xu, S., and Timme, S., "Robust and efficient adjoint solver for complex flow conditions," *Computers & Fluids*, Vol. 148, 2017, pp. 26–38.
- [13] Crouch, J. D., Garbaruk, A., and Magidov, D., "Predicting the onset of flow unsteadiness based on global instability," *Journal of Computational Physics*, Vol. 224, No. 2, 2007, pp. 924–940.
- [14] Williamson, C. H. K., "Oblique and parallel modes of the vortex shedding in the wake of a circular cylinder at low Reynolds numbers. J Fluid Mech 206: 579-627," *journal of fluid mechanics*, Vol. 206, No. -1, 1989, pp. 579–627.
- [15] Barkley, D., "Linear analysis of the cylinder wake mean flow," *Europhysics Letters*, Vol. 75, No. 5, 2006, p. 750.
- [16] Williamson, C. H. K., "Vortex Dynamics in the Cylinder Wake," *Annual Review of Fluid Mechanics*, Vol. 28, No. 1, 2003, pp. 477–539.
- [17] Strazisar, A. J., Wood, J. R., Hathaway, M. D., and Suder, K. L., "Laser anemometer measurements in a transonic axial-flow fan rotor," 1989.